Title

Testing the inference of creep on the northern Rodgers Creek fault, California, using ascending and descending persistent scatterer InSAR data

Journal

Journal of Geophysical Research: Solid Earth, 122(3)

ISSN

2169-9313

Authors

Jin, Lizhen
Funning, Gareth J

Publication Date

2017

DOI

10.1002/2016jb013535

Peer reviewed

JOURNAL OF GEOPHYSICAL RESEARCH, VOL. ???, XXXX, DOI:10.1029/,

Testing the inference of creep on the northern Rodgers Creek fault, California, using ascending and descending persistent scatterer InSAR data

Lizhen Jin[1]

Gareth J. Funning[1]

G. J. Funning, Department of Earth Sciences, University of California, 900 University Ave, Riverside, CA 92521, USA. (gareth@ucr.edu)

[1]Department of Earth Sciences, University of California, Riverside, California, USA.

Abstract.

We revisit the question of whether the Rodgers Creek fault in northern California is creeping, a question with implications for seismic hazard. Using imagery acquired by Envisat between 2003 and 2010, we process two persistent scatterer InSAR datasets, one from an ascending track and the other from a descending track, covering the northernmost segment of the Rodgers Creek fault between the cities of Santa Rosa and Healdsburg. The two different viewing geometries provided by the two different tracks allow us to distinguish vertical velocities, that may reflect nontectonic deformation processes, from fault-parallel velocities, that can be used to identify creep.

By measuring offsets in InSAR line-of-sight velocity from 12 fault-perpendicular profiles through both data sets, we identify seven locations where we have a high degree of confidence that creep is occurring (estimated creep rate is more than two standard deviations above zero). The preferred creep rates at these locations are in the range 1.9–6.7 mm/yr, consistent within uncertainty with alinement array measurements. Creep is probable ($P \geq 0.70$) at another three locations, defining a creeping zone ~ 20 km long in total, extending northwest from Santa Rosa. We also estimate the map patterns of fault-parallel and vertical velocities in the region covered by both data sets; these suggest that the Rodgers Creek fault immediately southeast of Santa Rosa remains locked.

1. Introduction

1.1. Fault creep and seismic hazards

Fault creep (also known as brittle creep and/or aseismic creep) is the sliding of upper crustal faults, constantly or episodically, in the absence of major earthquakes. It can be considered an alternate behavior to the stick-slip behavior that is thought to occur on most active faults [*Reid*, 1910]. The majority of reported fault creep cases on the continents lie within California [e.g. *Steinbrugge et al.*, 1960; *Cluff and Steinbrugge*, 1966; *Nason*, 1971; *Harsh et al.*, 1978; *Louie et al.*, 1985; *Bilham et al.*, 2004; *Funning et al.*, 2007; *Wisely et al.*, 2008; *McFarland et al.*, 2016], although creep has also been observed on the North Anatolian fault in Turkey for several decades [e.g. *Ambraseys*, 1970; *Cakir et al.*, 2005; *Bilham et al.*, 2016; *Rousset et al.*, 2016], and has been observed geodetically on the Longitudinal Valley fault (Taiwan), Haiyuan fault (China) and Chaman fault (Afghanistan) in the past decade [e.g. *Hsu et al.*, 2006; *Jolivet et al.*, 2012, 2013; *Fattahi and Amelung*, 2016]. Analogous asesimic slip within the depth range of expected seismogenic slip is also inferred on some subduction zone interfaces [e.g. *Wallace et al.*, 2004; *Bürgmann et al.*, 2005; *Kyriakopoulos and Newman*, 2016]. Multiple mechanisms have been proposed for fault creep, e.g. the presence of fluids at high pressures [e.g. *Sleep and Blanpied*, 1992; *Bedrosian et al.*, 2004] or weak minerals such as clays [e.g. *Lockner et al.*, 2011], serpentine [e.g. *Moore and Lockner*, 2013], or talc [*Moore and Rymer*, 2007] on the fault surface. It is not clear from our current state of knowledge whether geological conditions are sufficiently similar at the different locations where creep is observed that a single mechanism could explain all reported cases; it is possible that multiple mechanisms could be involved.

Since the portions of faults that creep are moving interseismically, rather than remaining locked, they accumulate less elastic strain energy than stick-slip faults. In most of the cases mentioned above, the average rate of creep is lower than the long-term slip rate of the fault estimated geologically, meaning that even though the fault is not locked, it is still accumulating strain [e.g. *Wisely et al.*, 2008; *Weldon et al.*, 2013]. However, if an earthquake were to occur on such a fault, we might expect a lower seismic moment release, compared with a fault of the same size that did not creep interseismically.

A second consideration is that of fault friction regime. In the nomenclature of rate-state friction [*Dieterich*, 1978; *Ruina*, 1983], we would consider stick-slip behavior 'velocity-weakening' – movement of the fault weakens the frictional resistance of the fault to movement, causing a positive feedback that promotes rapid, unstable seismic slip. Creep, on the other hand, implies 'velocity-strengthening' behavior – frictional strength of the fault increases with fault slip rate, acting to suppress rapid fault slip and promote stable sliding. There is evidence to suggest that regions of faults with different frictional regimes persist throughout the earthquake cycle. This can be seen in geodetic data from multiple earthquake cycles on the Parkfield segment of the San Andreas fault, where an asperity shown to be responsible for M$\sim$6 earthquakes in 1966 and 2004 is surrounded by regions that undergo creep during interseismic periods [*Murray and Langbein*, 2006]. In the week following the 2004 earthquake, the creeping portions of the fault released their accumulated elastic strain energy through accelerated postseismic creep [*Johanson et al.*, 2006]. The implication is that creeping fault segments may additionally act as barriers to earthquake rupture, and thus reduce the seismic hazard. In the seismic hazard estimates computed for California, such as UCERF3, this moment-reducing effect is accounted for by scaling seismic moments of potential earthquakes by a coefficient R, where $R \leq 1$ [*Field et al.*, 2014].

Finally, another hazard that has been observed in association with coseismic rupture in California, particularly on faults that were previously known to undergo surface creep, is postseismic fault slip, or 'afterslip'. Continued surface fault slip in the days or weeks that follow an earthquake can locally exceed the slip experienced during the earthquake, as observed in the 2014 South Napa, California event [e.g. *Lienkaemper et al.*, 2016; *Floyd et al.*, 2016], causing ongoing or repeat damage to fault-crossing infrastructure. In the event of a major earthquake on a creeping fault, we would anticipate a similar hazard in the weeks that followed.

In order to correctly characterize both seismic and postseismic hazards, therefore, it is important to know if, and if so, where, a fault is creeping. In this study, we attempt to answer this question for a potentially hazardous fault in northern California, using persistent scatterer InSAR data from multiple viewing geometries.

1.2. The Rodgers Creek fault

The Rodgers Creek fault extends for over 70 km in the northern San Francisco Bay area (hereafter 'North Bay') in northern California. Along with its along-strike neighbors – the Hayward fault, located to its southeast, and the Maacama fault, located to its northwest – the Rodgers Creek fault is estimated, on the basis of geodetic data, to accommodate a significant proportion (between 15 and 25 percent) of the relative motion between the Pacific plate and the Sierra Nevada-Great Valley block to the east, equivalent to a long-term slip rate of 6–10 mm/yr [e.g. *Prescott et al.*, 2001; *d'Alessio et al.*, 2005; *Funning et al.*, 2007; *Field et al.*, 2014; *Floyd et al.*, 2014]. Given this strain accumulation rate, the lack of historic earthquake ruptures along the fault, its unruptured length and the possibility of a joint rupture with the Hayward fault, the fault is considered the most dangerous in the region. Seismic hazard analyses suggest a 32% probability of a significant ($M > 6.7$) rupture in the next 30 years [*Field et al.*, 2014]. Such an earthquake could imperil the heavily populated San Francisco Bay area, close to the southern end of the fault; in addition, the fault also passes through the center of Santa Rosa, the largest and most populous city in the North Bay, and is close to communities in the Sonoma and Napa valleys, all of which would be strongly affected by such an event, drawing a sharp focus on the need to understand the behavior of the fault in detail.

Since written records began in the late 18th Century, there have been no major earthquakes on the Rodgers Creek fault. The most significant events in recent decades were a pair of M 5.5 events in Santa Rosa in 1969 [*Wong and Bott*, 1995]. Paleoseismic studies have shown that the most recent major event occurred approximately 235–296 years ago [*Hecker et al.*, 2005], and involved slip of $\sim$ 2 m [*Budding et al.*, 1991; *Hecker et al.*, 2005], consistent with a M$\sim$ 7 event if standard earthquake scaling relationships are assumed [e.g. *Wells and Coppersmith*, 1994]. Other trenches located between Windsor and Healdsburg suggest that the fault has been active in Holocene time along that segment of the fault [*Hecker et al.*, 2005]. If the slip rate for the fault were at the upper end of the 6.4–10.4 mm/yr range estimated from paleoseismic work by *Schwartz et al.* [1992], the fault could already have exceeded the time required to reload for a repeat of the most recent event.

1.3. Previous evidence for creep on the Hayward-Rodgers Creek-Maacama fault system

There is extensive observational evidence for shallow aseismic creep on both the Hayward and Maacama faults. This includes observations of offsets of cultural features such as curbs, road markings, walls and fences [e.g. *Cluff and Steinbrugge*, 1966; *Lienkaemper*, 2006], alinement array measurements [short (50–250 m) baseline, cross-fault theodolite measurements, e.g. *Galehouse and Lienkaemper*, 2003; *McFarland et al.*, 2016], and creepmeter observations [e.g. *Bilham et al.*, 2004]. Given the location of the Rodgers Creek fault in between these two creeping faults along-strike, it was speculated for many years that the Rodgers Creek fault might also creep. Prior to the last decade, evidence for creep was limited and equivocal, with no reported cultural offset features and only a few alinement arrays, whose data did not support creep [e.g. *Galehouse and Lienkaemper*, 2003]. Such data did not rule out creep entirely, however, since the distribution of alinement arrays was sparse – prior to 2002, there were only two alinement arrays along the whole of the fault. In addition, the low density of population along much of the fault trace meant that there were few cultural features in those areas that could be offset. If creep were spatially discontinuous, it may not have been captured by that set of observations.

The advent of high precision InSAR deformation measurements based upon long data time series [e.g. *Ferretti et al.*, 2001; *Berardino et al.*, 2002; *Hooper et al.*, 2004] has provided a means of characterizing and mapping slow-moving deformation sources across large areas. These techniques rely upon spatiotemporal filtering of InSAR time series to separate the signal due to deformation, which is correlated in time, from that due to atmospheric noise, which is correlated in space, but not in time. Such analyses permit deformation measurements to be made at precisions of 1.0 mm/yr or better in the line-of-sight direction of the satellite [*Ferretti*, 2014]. For most satellite applications of InSAR, this gives sensitivity to deformation in the vertical and E-W directions.

A change in deformation velocity across the northern Rodgers Creek fault in such a data set spanning the interval 1992–2000 led *Funning et al.* [2007] to infer that the fault was creeping along a segment between the cities of Santa Rosa and Healdsburg at rates of up to 4–6 mm/yr, using both direct estimates of the surface offset rate from the data, and elastic dislocation modeling. This interpretation was controversial, given the lack of surficial evidence mentioned above, and also given the possibility that the fault-bounded velocity change observed could also be consistent with a relative vertical motion across the fault. Subsequent field identification of offset curbs along a secondary trace of the Rodgers Creek fault in Santa Rosa (Suzanne Hecker, personal communication, 2008) and ongoing alinement array survey measurements [*McFarland et al.*, 2016] have provided tentative, but by no means definitive, support for the occurrence of creep along the northern portion of the fault, albeit at a significantly slower rate (< 2 mm/yr).

There are three potential explanations for such a difference in rate between the InSAR estimates and the alinement array estimates, assuming that neither of the rate estimates was erroneous. If, for instance, the observed cross-fault velocity change were a combination of horizontal and vertical motion, rather than the purely horizontal motions assumed by *Funning et al.* [2007], it is possible that the majority of the observed line-of-sight deformation could be due to vertical motions, and the creep rate could be small. Alternatively, the creep rate could be variable on a decadal time scale, such that the InSAR estimates, from data acquired in the 1990s, could be larger than the more recently acquired alinement array data. Finally, the two methods are sensitive to creep over different depth ranges on the fault, and therefore any differences between them may reflect different creep rates at different depths.

In this study, we further test the inference of creep on the northern Rodgers Creek using a later, and more comprehensive InSAR dataset than that used by *Funning et al.* [2007]. Specifically, we use data from both ascending and descending viewing geometries, with the advantage that the vertical and horizontal components of deformation can be distinguished.

2. Observations

2.1. Data processing

Persistent scatterer (PS) InSAR methods provide a means for measuring ongoing deformation of targets on the ground, typically with a better spatial coverage than is achievable using conventional InSAR. By identifying PS – targets on the ground that are phase-stable (i.e. the phase response of the target to incident radar waves does not change) over the period of time covered by the SAR dataset – it is possible to identify pixels with coherent deformation signals even when they are surrounded by heavy vegetation, and to make precise estimates of deformation rates with the effects of atmospheric noise and other errors mitigated [see *Hooper et al.*, 2012, for a full review]. These capabilities make PS methods particularly useful in inhabited vegetated areas such as the North Bay.

A number of different software codes exist that implement persistent scatterer approaches [e.g. *Ferretti et al.*, 2001; *Hooper et al.*, 2004; *Kampes*, 2006]. Here we use the Stanford Method for Persistent Scatterers code [StaMPS; *Hooper et al.*, 2004, 2007; *Hooper*, 2010, https://homepages.see.leeds.ac.uk/ earahoo/stamps/] to produce a displacement time series for each stable pixel, giving its displacement (with respect to a reference pixel) at each observation date resolved into the satellite line-of-sight (LOS), with the effects of spatially-correlated tropospheric noise, and orbit and pixel height errors estimated and removed. From these displacement time series, a best-fitting LOS velocity is estimated for each PS.

We process, in this way, two datasets from two different viewing geometries (ascending and descending tracks) acquired by the ASAR (Advanced Synthetic Aperture Radar) instrument onboard Envisat (Environment Satellite, operated by the European Space Agency), which will be described below. Data are geocoded and topographic artifacts removed using a 30 m resolution digital elevation model from NASA [*Farr and Kobrick*, 2000].

2.2. Descending track data

Our descending track dataset comprises 33 Envisat ASAR images (track 342, frame 2835, see Table S1 for details) acquired between March 2003 and May 2010. We use a subset of the full frame (Figure 1), centered on the area of interest along the northern Rodgers Creek fault, in order to expedite processing. Using the StaMPS code, we identify 112,800 PS in a rectangular area of approximately 30 km $\times$ 50 km over the majority of the active fault trace. These are plotted in Figure 2 with negative velocities (indicating motion away from the satellite) colored red and positive velocities (towards the satellite) colored blue.

The largest positive PS velocities in the dataset appear on the northwest corner of the map (location V1 in Figure 2), northeast of the town of Cloverdale near the Maacama fault, a deformation of the ground towards the satellite of $\sim$ 6 mm/yr. The largest negative

PS velocities of -9 mm/yr cluster approximately 10 km to the east of this peak, at the southern edge of The Geysers, a major geothermal field (location V2). A concentrated area of positive velocities can be seen aroun 10–15 km south of Santa Rosa in an area known as the Cotati basin (location V3). We will discuss the implications of this signal below. Near the city of Santa Rosa and further north, the color scale changes abruptly from green to blue crossing the fault from west to east, a line-of-sight velocity change of $\sim 1 - 2$ mm/yr that could be explained by right-lateral horizontal motions localized on the fault (i.e. shallow creep) or differential vertical motions across the fault (with the east side of the fault uplifting with respect to the west side), or a combination of both, as we shall investigate below.

2.3. Ascending track data

We additionally process an ascending track dataset of 39 Envisat ASAR images (track 478, frame 765, see Table S2 for details) acquired between August 2003 and April 2010 using the StaMPS methodology. As in the case of the descending track data, we use a subset of the full frame (Figure 1), centered on the area of interest along the northern Rodgers Creek fault, in order to expedite processing. We identify 100,596 persistent scatterers in our area of interest (Figure 2). The footprint of this dataset covers a slightly different area to the track 342 dataset, such that Cloverdale and The Geysers (locations V1 and V2) are not included. However we do see high positive velocities around the Cotati basin (location V3), similar to the track 342 data. Cross-fault changes in velocity are less pronounced than in the track 342 data, and more variable in terms of sign.

3. Analysis and modeling

3.1. Decomposing line-of-sight velocities into fault-parallel and vertical motions

InSAR measurements are inherently one-dimensional in that they measure changes of range (satellite-ground target path length) in a single viewing geometry. Even with two such independent 'range change' measurements, each from a different viewing geometry, it is not possible to recover the full (three-dimensional) displacement vector – this typically requires a measurement of the surface displacement in the along-track direction to complement the two range change observations [e.g. *Funning et al.*, 2005]. In the case of the proposed creep segment of the Rodgers Creek fault, the rate of displacement is too small to be measurable using the azimuth offset technique [e.g. *Michel et al.*, 1999; *Peltzer et al.*, 1999; *Jónsson et al.*, 2002].

In this case, with two independent measurements, we can only estimate two components of motion. Given the expectation that close to a creeping fault, horizontal deformation will be dominated by fault-parallel motions, we choose therefore to resolve horizontal deformation into the direction of the fault strike, so that we can resolve fault creep directly. The decomposition of ascending and descending InSAR displacements into displacements in the vertical direction and an arbitrary horizontal direction can be accomplished by the following procedure:

Measured deformation in the satellite line-of-sight (in this case, the range change rate), $\dot{r}$ can be expressed as the product of the three-component vector of the ground deformation, $\mathbf{v}$ $(= [v_x \; v_y \; v_z])$, and the unit pointing vector, i.e. a vector pointing from the satellite to the ground target, $\hat{\mathbf{p}}$ $(= [\hat{p}_x \; \hat{p}_y \; \hat{p}_z] = [\cos\phi \sin\lambda \quad -\sin\phi \sin\lambda \quad -\cos\lambda])$, where ϕ is the satellite heading azimuth, and λ is the incidence angle at the location of the ground target. With our two independent data sets from different viewing geometries, we would expect different range change rate estimates and different pointing vectors, and can thus write two equations in terms of $\mathbf{v}$:

$$\dot{r}_a = \hat{\mathbf{p}}_a \cdot \mathbf{v} \tag{1}$$

$$\dot{r}_d = \hat{\mathbf{p}}_d \cdot \mathbf{v}, \tag{2}$$

where the 'a' and 'd' subscripts denote the quantities associated with ascending and descending track data, respectively.

We next decompose the ground deformation velocity $\mathbf{v}$ into two components – a vertical component with amplitude v_z and a horizontal component with amplitude v_h in a selected direction defined by the two-dimensional unit vector $\hat{\mathbf{v}}_h = [\sin\gamma \cos\gamma]$, representing the unit vector in the average fault strike direction, γ. The range-change rates for these decomposed velocities are given by:

$$\dot{r}_a = v_h(\hat{\mathbf{p}}'_a \cdot \hat{\mathbf{v}}_{\mathbf{h}}) + v_z \hat{p}_{za} \tag{3}$$

$$\dot{r}_d = v_h(\hat{\mathbf{p}}'_d \cdot \hat{\mathbf{v}}_{\mathbf{h}}) + v_z \hat{p}_{zd}, \tag{4}$$

where $\hat{\mathbf{p}}'_a$ and $\hat{\mathbf{p}}'_d$ are two-dimensional vectors containing the horizontal components of the ascending and descending unit pointing vectors, respectively, and $\hat{p}_{za}$ and $\hat{p}_{zd}$ are the corresponding vertical components of the unit pointing vectors.

We can recast these simultaneous equations as normal equations in matrix form:

$$\mathbf{Am} = \dot{\mathbf{r}} + \mathbf{e} \tag{5}$$

where

$$\mathbf{A} = \begin{pmatrix} \hat{\mathbf{p}}'_a \cdot \hat{\mathbf{v}}_{\mathbf{h}} & \hat{p}_{za} \\ \hat{\mathbf{p}}'_d \cdot \hat{\mathbf{v}}_{\mathbf{h}} & \hat{p}_{zd} \end{pmatrix}, \tag{6}$$

$\mathbf{m} = [v_h \ v_z]^T$, and $\dot{\mathbf{r}} = [\dot{r}_a \ \dot{r}_d]^T$. The vector $\mathbf{e} = [e_a \ e_d]^T$ contains the uncertainties in $\dot{r}_a$ and $\dot{r}_d$, which can be estimated from the standard deviation of the residual of the linear velocity trend to the PS time series.

We invert this system of equations using standard least-squares methods, weighting by the inverse of the variances of the range-change rates, in order to obtain best-fitting estimates of $\mathbf{m}$. We construct a variance-covariance matrix, $\mathbf{E}$, such that:

$$\mathbf{E} = \begin{pmatrix} e_a^2 & 0 \\ 0 & e_d^2 \end{pmatrix}. \tag{7}$$

Then, the best fitting model velocities are given by

$$\mathbf{m} = (\mathbf{A^T E^{-1} A})^{-1} \mathbf{A^T E^{-1}} \dot{\mathbf{r}}, \tag{8}$$

with corresponding model velocity covariances given by

$$\mathbf{C} = (\mathbf{A^T E^{-1} A})^{-1}. \tag{9}$$

We apply this scheme to our data in two different ways. First, LOS offset rates, estimated from profiles through both our InSAR data sets, are used to estimate the fault-parallel and vertical offset rates at discrete intervals along the fault. Second, we apply this scheme, pixel by pixel, to both InSAR datasets downsampled onto a common grid, in order to find the map pattern of fault-parallel and vertical deformation.

3.2. Estimating creep rates from cross-fault profiles

We first apply the above decomposition of InSAR LOS displacements into fault-parallel and vertical deformation rates to cross-fault profile data. PS velocities from both SAR tracks are sampled at 2.5 km intervals along the northern section of the Rodgers Creek fault, along 15 km-long strike-perpendicular profiles (Figure 2). The profile locations, orientations and lengths are based on the previous study of *Funning et al.* [2007], to facilitate comparisons between the results of the two studies. We then estimate surface fault offset rates along each profile, using a modified version of the method employed by *Funning et al.* [2007], shown in Figure 3, where a pair of straight lines with a common gradient, but different y-axis intercepts are fitted to the profile data on either side of the fault. The difference in y-axis offset between the best-fit lines on either side of the fault provides a measure of the LOS velocity step (if any) across it. By fitting a common gradient on both sides of the profile, we mitigate any regional gradient that may be present in the data due to interseismic strain accumulation across the plate boundary system, and any residual orbital errors. To account for local variations in fault strike and the location of the surface trace, data within a zone 100 m either side of the fault are excluded. We tested different window lengths of data either side of the fault to which to fit these straight lines, between 2 and 5 km, to see which would be most appropriate (Figures 4, S1–S4). We choose to use data within 4 km of the fault in our analysis; we select this length scale on the basis of the uncertainties of the LOS offset rate estimates, and because it is significantly larger than the expected scale of the local basin features in the area [< 1 km; *Hecker et al.*, 2016], thus reducing possible effects of biasing our estimates by nontectonic motions within those basins.

In the modified methodology used here, we simultaneously apply the analysis to the data from the ascending and descending tracks, using the two LOS velocity steps to estimate horizontal (fault strike-parallel) and vertical offset rates for each profile, using the method described above. The average formal LOS velocity uncertainties estimated from our PS analysis ($|e_a| = |e_d| = 1.0$ mm/yr) are propagated through these calculations in order to provide an estimate of the model uncertainties; we estimate the standard deviation of the scatter in the profiles as a whole to be ~ 0.8, similar to the formal uncertainties in our data.

In all, we analyze 12 profiles along the previously identified creeping zone of the Rodgers Creek fault that had sufficient PS in both data sets to measure LOS offsets at the fault. These profiles, detrended using the best-fitting linear gradient in each case, are shown in Figure 4. In these, we identify evidence for both vertical motions (similar pattern of velocities in both descending and ascending data sets) and fault-parallel creep (significantly greater LOS offset in the descending track data than in the ascending track data). An example of a feature consistent with vertical motions can be seen in profiles J–J' and K–K' at an along-profile distance of ~ 2500 m. Here, a small peak in LOS velocity of 2–3 mm/yr above the 'background' deformation west of the fault, and approximately 1000 m wide, can be distinguished in both descending and ascending data sets, consistent with localized uplift. Conversely, the data from profile H–H' show a LOS offset of 1.3 ± 0.6 mm/yr in the descending track data and a significantly smaller offset of 0.1 ± 0.8 mm/yr in the ascending track data (uncertainties quoted are 2σ, i.e. two standard deviations). Applying the velocity decomposition described above to these offset rates yields a horizontal, fault-parallel offset rate of 2.6 ± 2.2 mm/yr and a east side-up vertical offset rate of 0.5 ± 0.6 mm/yr (1σ uncertainties), suggesting that this particular location is dominated by fault-parallel creep with a possible minor component of uplift.

Figure 5 and Table 1 show the along-strike variation in fault-parallel and vertical offset rates estimated in this way from our profile offsets. For seven out of the 12 profiles, the estimated creep rate is more than 2σ (two standard deviations) above zero; we have high confidence in the occurrence of creep at these locations, which are within Santa

Rosa (profiles K–K' and L–L'), in a central zone ~ 5 km to the northwest of Santa Rosa (profiles E–E', F–F', G–G' and H–H') and immediately southeast of Healdsburg (profile C–C'). For some of the other profiles (e.g. the pairs of profiles either side of the central zone), the estimated fault-parallel rate values and uncertainties are between 1σ and 2σ above zero. We estimate the one-tail probabilities for right-lateral creep (i.e. a creep rate greater than zero), based on our estimated creep values and standard deviations for these sites (Table 1). At three of the sites (profiles D–D', I–I' and J–J'), these probabilities are suggestive of the occurrence of creep ($P \geq 0.70$), albeit at a lower level of confidence. On the other hand, the two profiles at the northwest end of the fault (A–A', B–B'), near Healdsburg, have a substantially lower probability of right-lateral creep ($P \leq 0.33$), and we do not consider them to show creep.

Overall, where we can confidently resolve them, our preferred creep rates along the northern Rodgers Creek fault are in the range 1.9–6.7 mm/yr. In contrast, vertical offset rates are generally smaller, in the range of -1.8 to 0.9 mm/yr. There is a suggestion of an anticorrelation between high creep rates and negative uplift rates along the central portion of the fault segment (Figure 5), but this is not reproduced at the southeastern end of the fault, in Santa Rosa, where creep is also significant.

3.3. The map pattern of fault-parallel and vertical motions

We next investigate the spatial extent of fault creep and its discrimination from vertical deformation by looking at their patterns in map view. In order to achieve this, we first sample both ascending and descending data points onto the same regular grid with a spacing of 0.001° in longitude and latitude (approximately 100 m spacing) using a nearest neighbor procedure. Next, each of our InSAR data sets is flattened by subtracting a best-fitting linear ramp, and referenced to a common point, in order to account for plate boundary-scale deformation signals and long-wavelength errors, such as incorrectly modeled satellite orbits. One implication of this flattening procedure is that the horizontal and vertical motions we obtain are only valid over short length scales (< 5 km), the flattening acting effectively as a high-pass filter on deformation features. However our main focus is on laterally abrupt changes in deformation rate associated with fault creep, which can still be resolved under this scheme. The velocity decomposition is then applied to every grid point with collocated ascending and descending LOS velocities. An azimuth of 135°, is used to approximate the strike of the northern Rodgers Creek fault, for the purposes of estimating horizontal, fault-parallel velocities.

The results of the velocity decomposition are shown in map view in Figure 6, and in profile form in Figure S5. In general, the pattern of vertical velocities is smooth across the area of interest, whereas the map of fault-parallel velocities has a noisier appearance. There are several likely reasons for this. First, the $\sim 23°$ incidence angle for the Envisat data used in this study means that the data have a significantly greater sensitivity to vertical motions than horizontal. Thus, horizontal motions' contributions to LOS velocity will be closer to the noise floor than the corresponding contributions from vertical motions, and so the recovered horizontal velocities will appear noisier. Another consequence of this lower sensitivity to horizontal motions is that, in effect, a larger 'gain' must be applied to the horizontal components of LOS velocity when estimating the fault-parallel velocity, thus amplifying any noise that they contain. Finally, in order to achieve the velocity decomposition, we have assumed that all horizontal velocities must occur in the fault-parallel direction. While this is a reasonable assumption when focusing on shallow fault slip due to creep, it is much less safe when considering the other possible sources of horizontal deformation that may be present in the data (e.g. landsliding, expansion/contraction of aquifers). Therefore, although we can identify some features of fault creep in our fault-parallel velocity map, some caution is advised when interpreting off-fault horizontal deformation features.

As might be expected, we see evidence for a near-field change in fault-parallel velocities along the section of the northern Rodgers Creek fault where creep is inferred from cross-fault LOS velocity profiles. The amplitude of this velocity step varies along strike, from ~ 5 mm/yr within Santa Rosa, to rates of 2–3 mm/yr seen 5–10 km to the northwest. We can also identify relative subsidence of ~ 2 mm/yr east of the Rodgers Creek fault trace along profiles E–E' and F–F' (Figure S5), consistent with the estimates of relative vertical motions made from our profile offsets (Figure 4). Immediately southeast of Santa Rosa, there is no resolvable velocity change in fault-parallel velocity, indicating that creep does not extend further in that direction, although there is limited near-fault coverage in that area. Coverage is even more limited near the Maacama fault, and therefore it is not possible with these data to assess whether there is shallow creep along the southernmost portion of its mapped trace.

The principal feature of the vertical deformation map is a rhomboidal area of uplift, approximately 6 km wide with an amplitude of 6 mm/yr, located ~ 10 km south of Santa Rosa. In our previous study, based on data acquired by the European Space Agency ERS satellites between 1992 and 2000, the same area was marked by range increase consistent with subsidence, and was interpreted as subsidence due to net groundwater withdrawal

[*Funning et al.*, 2007]. The uplift apparent in this data set, spanning 2003–2010, suggests that this period was marked by net groundwater recharge.

Elsewhere, a series of small-scale subsidence features can be identified, including a pair of areas subsiding at rates of 2 mm/yr, $\sim$ 2 km across that lie approximately 1 km either side of the Rodgers Creek fault trace within Santa Rosa. It is not clear what these features represent, but perhaps they could be related to the releasing bend on the Rodgers Creek fault within Santa Rosa, for which a number of secondary normal fault structures have been identified that may bound local basins and topographic depressions [*Hecker et al.*, 2016]. Other subsidence features in the region have been attributed to fluid withdrawal and/or sediment compaction or settling [e.g. *Ferretti et al.*, 2004; *Funning et al.*, 2007], but it is less clear which of these processes should occur in the area immediately surrounding the fault. The presence of thick basin sediments (2 km or greater) in the plain to the SW of Santa Rosa has been inferred from geophysical mapping [e.g. *Langenheim et al.*, 2006] and from the large ground motions in the area that accompanied the great 1906 earthquake on the San Andreas fault [*McPhee et al.*, 2007], but the basin thickness is significantly reduced (to 500 m or less) in the vicinity of the Rodgers Creek fault.

4. Discussion

Our analysis of the persistent scatterer InSAR-processed ascending and descending Envisat data surrounding the northern Rodgers Creek reveals that at seven out of 12 locations we are confident that we can resolve creep at rates of 1.9–6.7 mm/yr. At three more locations, the probability of a creep rate greater than zero is at least 0.7. Here we explore the implications of these results in the context of previous results, and also in terms of seismic hazard.

4.1. Comparison with other studies of fault creep on the Rodgers Creek fault

As we described above, there have been a few previous studies that estimate the creep rate of the Rodgers Creek fault. We highlight here two that are particularly appropriate for comparison.

McFarland et al. [2016] measured a series of alinement arrays as part of an ongoing project of monitoring along the Rodgers Creek fault and other major structures in northern California. Although few of these observations span the entire period of observation of the Envisat data used in this study, several of them do overlap with the later portion of that observation period, permitting a tentative comparison. We plot the along-strike variations in horizontal creep rates from our InSAR profile analysis along with the alinement array rates in Figure 5.

At three out of four of the alinement array sites the 2σ uncertainty bounds for the two sets of creep rate estimates overlap, suggesting that the two observation sets are generally compatible, albeit with a few caveats or points of note: First, the highest creep rate from the alinement array data set, from Mark West Springs Rd, northwest of Santa Rosa (site RCMW) has uncertainties that partially overlap with the nearest creep rate estimate from InSAR (profile I–I'), suggesting that the InSAR estimate could be an underestimate at that location. Second, the longest-lived, and therefore most precise, alinement array site at Solano Drive in Santa Rosa (site RCSD) has a significantly lower creep rate (1.44 ± 0.14 mm/yr) than is estimated at the nearest InSAR profile (L–L'; 6.7 ± 1.4 mm/yr; both sets of uncertainties quoted at the two-sigma level). This difference might not necessarily reflect an inconsistency between the two data sets, given the location of RCSD at the very southeastern end of the creeping zone as identified in our fault-parallel deformation map, close to the transition to zero creep. Third, we have included the creep rate estimated at the alinement array at Fountaingrove Blvd in Santa Rosa (site RCFG) between 2008 and 2011 in our comparison. Measurements at this site were considered problematic by *McFarland et al.* [2016], suggesting a negative (i.e. left-lateral) creep rate, indistinguishable within error from zero, which prompted a reinstallation of one of the survey markers in 2014. Interestingly, however, the InSAR result for the nearest profile (J–J') also suggests a creep rate that is zero within 2σ error, implying that a near-zero rate may be permitted at that site.

A final, and most important, caveat is that the two observation sets have different apertures, i.e. they measure the effect of creep over different distances – over 250 m or less for alinement arrays, versus over several kilometers for InSAR. This implies that they are sensitive to creep over different depth ranges on the fault (the upper few tens of meters for alinement arrays, the upper few kilometers for InSAR).

A more direct comparison can be made with our earlier study [*Funning et al.*, 2007], which also used persistent scatterer InSAR data to infer creep rates on the northern Rodgers Creek fault. The primary differences between that study and this were that data from a different satellite system were used (the European Space Agency satellites ERS-1 and ERS-2), spanning a different time interval (1992–2001), and that given different data acqusition priorities during this earlier period, only descending track data were available in sufficient quantities for persistent scatterer analysis, meaning that creep rate estimates were made by assuming any observed LOS offsets could be attributed to horizontal fault motions, rather than by decomposing observations from two lines-of-sight into fault-parallel and vertical components. Despite these differences, since the ERS and Envisat satellites shared common orbital tracks and imaging swaths and a common imaging geometry (i.e. the same radar incidence angles), the data from the earlier study should be similarly sensitive to creep as the descending track (track 342) data used in this study, and a comparison can be made on that basis. The two studies used the same profile azimuths and lengths (15 km, centered approximately on the fault) and the same method of estimating LOS offset with one difference – the earlier study collapsed data from 5 km wide 'bins' onto profile lines running through their centers, whereas the current study divided those original bins in half, producing a greater number of narrower, more closely spaced profiles.

The upper panel of Figure 7 shows comparisons of both the estimated creep rates from *Funning et al.* [2007] and this study. We will focus here first on the creep rate comparison. Over the majority of the fault segment considered, the preferred creep rate values from the 2007 study are higher than the values from this study, but the difference is unlikely to be significant – the two-sigma uncertainty bounds from each study show substantial overlap, suggesting that for the most part the creep rate estimates are consistent within error.

There is, however, one location where the higher creep rate estimate from the 2007 study is significantly higher than that from the current study – in the distance range 16–23 km along-strike (measured southeastwards from the profile A–A' close to the city of Healdsburg). Here, a creep rate of 6.0 ± 1.2 mm/yr from the earlier study is about 5 mm/yr higher than the estimates made in the current study, whose uncertainties overlap with zero creep rate. This is close to the location of the alinement array RCMW [*McFarland et al.*, 2016, Figure S2], whose creep rate estimate (4.37 ± 1.34 mm/yr) is also likely higher than that of our current study, but also spanned a different time interval (2008–2015). The difference in estimated creep rate between the two InSAR studies could be taken to imply that the creep rate at that location could be variable on approximately decadal time scales. We shall explore this possibility below.

4.2. The possibility of time-variable creep

Time dependence in fault creep is observed in a number of locations where creep has been monitored in the longer term [e.g. *McFarland et al.*, 2016; *Rousset et al.*, 2016]. Alinement arrays monitored by groups from the US Geological Survey an San Francisco State University have revealed a complex picture of fault creep for over 30 years in the San Francisco Bay Area [*Galehouse and Lienkaemper*, 2003; *McFarland et al.*, 2016]. A number of the faults monitored, including the northern Calaveras fault at San Ramon, and the Hayward fault in Fremont, have shown large variations in creep rate in that time. In San Ramon, the Calaveras fault creeps in an episodic fashion, with multi-year periods of low creep, followed by short periods of faster creep [*McFarland et al.*, 2016]. In Fremont, the Hayward fault was observed to cease creeping (and in some cases, even to slip left-laterally) following the 1989 Loma Prieta earthquake [*Lienkaemper et al.*, 1991], and then, after several years of stasis, the fault 'caught up' with its multidecadal rate with a slow slip event in 1996 [*Lienkaemper et al.*, 1997]. Given these other instances of variable creep rate over time, it is quite plausible that the Rodgers Creek fault could exhibit decadal variations in creep rate. However, it is not clear that our data fully support this interpretation.

The lower panel of Figure 7 shows the along-strike distribution of LOS velocity offsets from the *Funning et al.* [2007] descending track 342 data, compared with the corresponding offsets from this study. Along most of the fault segment, the LOS velocity offsets agree well within error of each other, except for a difference of $\sim 1-2$ mm/yr located between 10 and 15 km along-strike. Considering the separation between the two sets of creep rate estimates between 16 and 23 km along-strike described above, it is perhaps a little surprising that the LOS velocity offsets in the same interval agree so closely. The implication is that the difference in creep rate that is recovered from the data is more likely due to the difference in methodology or assumptions (i.e. assuming that the descending track LOS offsets were entirely due to fault-parallel velocity offsets in the 2007 study), rather than representing a change in creep rate. On the other hand, at the location where there is a difference in LOS velocity offset between the two data sets (10–15 km along-strike), perhaps a stronger case could be made for a temporal change in velocity, assuming that the proportions of fault-parallel and vertical velocities remained approximately constant over the two decades, although we do not have an ascending track data set spanning the period 1992-2001 to verify this.

4.3. Are there lithological associations with creep on the Rodgers Creek fault?

As mentioned above, several plausible mechanisms for creep have been proposed, several of which involve the presence of weak geological materials within fault gouge [e.g. *Moore and Rymer*, 2007; *Lockner et al.*, 2011; *Moore and Lockner*, 2013]. At the San Andreas Fault Observatory at Depth, the gouges associated with the creeping fault zones were rich in magnesium-rich saponite clays thought to be derived from metasomatic reactions between ultramafic rocks within the fault zone and the quartzofeldspathic wall rocks that border them [*Lockner et al.*, 2011]. With confirmation of the occurrence of creep on the northern Rodgers Creek fault, we raise the question: can we identify any similar lithological association here?

The city of Santa Rosa is situated on a Holocene alluvial fan [*McLaughlin et al.*, 2008], largely coincident with the releasing bend in the Rodgers Creek fault that marks the start of creep. Holocene alluvium abuts most of the creeping section of the fault to its west, except for a 5 km segment immediately northwest of the releasing bend where Pliocene sediments of the Petaluma formation are exposed. To the east of the Rodgers Creek fault are Pliocene-age Sonoma volcanics, and, further to the northwest, Plio-Pleistocene fluvial gravels [*Graymer et al.*, 2006; *McLaughlin et al.*, 2008]. No ultramafic rocks have been observed in contact with the fault at the surface where we are confident of the occurrence of creep, although there is mapped outcrop of Great Valley sequence serpentinite along the fault north of Healdsburg (approximately at the location of profile B–B' in Figure 2), and also a series of mapped slivers of the same unit striking parallel to the fault at distances of 1.5–9 km to the east [*Graymer et al.*, 2006]. Further information on the subsurface geometries of these slivers would be required to assess whether they may intersect with the Rodgers Creek fault at depth, and be a viable cause of the shallow creep we observe.

More intriguingly, *Hecker et al.* [2016] in their study of the releasing bend in Santa Rosa present geophysical data consistent with the presence of ophiolitic material in close proximity to the fault at depth. Paired positive gravity and magnetic anomalies, approximately 3 km long and 2 km wide, aligned with the fault trace and located immediately to its east, are consistent with a dense, magnetite-rich unit beneath Santa Rosa. Given its coincidence with the southern end of the creeping segment, we suggest that this feature warrants further investigation as a potential cause.

4.4. Implications for seismic hazard

The confirmed presence of surface creep on the northern Rodgers Creek fault, extending northwestwards from Santa Rosa, has implications for seismic hazard assessment. Dynamic rupture modeling experiments targeted at similar, neighboring structures such as the Bartlett Springs fault, have shown that creeping areas can channel fault ruptures at depth or arrest them completely [e.g. *Lozos et al.*, 2015]. This would likely reduce the expected strong shaking, although detailed scenario modeling of the Rodgers Creek fault would be required to quantify precisely by how much. The suggestion from previous experiments is that the down-dip width of the creeping areas plays a major role in selecting between these possible outcomes, with wider (deeper) creeping areas more likely to arrest dynamic rupture [*Lozos et al.*, 2015]. The sparse off-fault InSAR data coverage in this heavily vegetated region makes it very challenging to constrain that depth from InSAR alone in this case. Additional constraints on creep at depth, from GPS or from characteristic repeating earthquake sequences would likely enable a more accurate estimate of the seismic potential of the Rodgers Creek fault in this area in future.

Finally, earthquakes on other creeping faults, such as the Parkfield segment of the San Andreas fault, have been associated with rapid afterslip afterward [e.g. *Johanson et al.*, 2006]. The prevalence of creep along the northern Rodgers Creek fault may imply a continuing afterslip hazard to fault-crossing infrastructure in the days or weeks following an earthquake in the area.

5. Conclusions

Our joint analysis of the ascending and descending track Envisat persistent scatterer InSAR data from 2003–2010 confirms that the northernmost segment of the Rodgers

Creek fault is creeping. By estimating offsets in profiles through both datasets, and then decomposing these offsets into their fault-parallel and vertical components, we are able to identify locations where the creep rate is significantly greater than zero. There are seven such locations, located up to 20 km northwest of the city of Santa Rosa, where the surface creep rate is more than two standard deviations above zero, at rates between 1.9 and 6.7 mm/yr, and thus we have a high degree of confidence that creep is occurring. At a further three locations, the surface creep is more than one standard deviation above zero, suggesting that creep is likely.

We also use the distributions of persistent scatterer velocities from both InSAR data sets to estimate the map pattern of fault-parallel and vertical displacements. From these, a picture emerges of cross-fault jumps in fault-parallel velocity extending northwest from Santa Rosa, as expected, but also an abrupt transition to a zone to the southwest where there is no such jump in velocity, indicating an absence of creep. The pattern of vertical velocities is smoother, reflecting a higher signal-to-noise ratio for vertical motions, and shows a prominent area of uplift in an area 10 km south of Santa Rosa where earlier data sets had shown subsidence [*Funning et al.*, 2007]. We interpret this feature as an aquifer that, during the observation period, was undergoing net recharge, and had previously experienced net discharge. We also identify areas of small-scale subsidence that in some cases may be related to local structure, such as a releasing bend in the Rodgers Creek fault in Santa Rosa.

Our estimated fault creep rates are comparable within error with estimates made using complementary methods, such as measurements of alinement arrays, but provide a higher resolution picture of the along-strike variations in creep rate. Comparisons with data sets spanning an earlier time period [1992-2001; *Funning et al.*, 2007] show that ascending track data are essential for the accurate estimation of creep rate. In one location, immediately NW of Santa Rosa, we find a significant difference in inferred creep rate between the 1990s [i.e. *Funning et al.*, 2007] and the 2000s (this study), yet when the descending track LOS offset data from the two studies are compared, we see very little difference. The implication is that the ascending track LOS offsets from the 2000s are consistent with a significant component of vertical motion at that location, and thus less fault-parallel velocity is required to produce the observed descending LOS offset. In other words, it is not always safe to assume a purely horizontal sense of motion for a fault-bounded offset signal. Similarly, without additional information, we are unable to assess whether a change in the descending LOS offset rate between the 1990s and the 2000s, at a location midway between Healdsburg and Santa Rosa, represents a change in the creep rate or whether it could instead be caused by a change in the sense of cross-fault motion (e.g. additional vertical motion due to a non-tectonic process). We would recommend that future studies of fault creep with InSAR take these possible ambiguities into account, and preferably use data from multiple viewing geometries to mitigate them.

Acknowledgments. This work was supported by NASA New Investigator Program award NNX08AV23G. Envisat data are copyrighted by the European Space Agency, and were made available through the Western North America InSAR Consortium (WInSAR) hosted at UNAVCO. The processed persistent scatterer InSAR data used in this study are available as supplementary materials. The public domain Generic Mapping Tools [*Wessel and Smith*, 1998] were used in the production of our figures. We thank two anonymous reviewers for constructive comments that have helped to improve the manuscript.

References

Ambraseys, N. (1970), Some characteristic features of the North Anatolian Fault Zone, *Tectonophys.*, *9*, 143–165.

Bedrosian, P. A., M. J. Unsworth, G. D. Egbert, and C. H. Thurber (2004), Geophysical images of the creeping segment of the San Andreas fault: implications for the role of crustal fluids in the earthquake process, *Tectonophys.*, *385*, 137–158.

Berardino, P., G. Fornaro, R. Lanari, and E. Sansosti (2002), A new algorithm for surface deformation monitoring based on small baseline differential SAR interferograms, *IEEE Trans. on Geoscience and Remote Sensing*, *45*(11), 3468–3480.

Bilham, R., N. Suszek, and N. Pinkney (2004), California creepmeters, *Seismol. Res. Lett.*, *75*, 481–492.

Bilham, R., H. Ozener, D. Mencin, A. Dogru, S. Ergintav, Z. Cakir, A. Aytun, B. Aktug, O. Yilmaz, W. Johnson, and G. Mattioli (2016), Surface creep on the North Anatolian fault at Ismetpasa, Turkey, 1944–2016, *J. Geophys. Res.*, *121*, doi: 10.1002/2016JB013394.

Budding, K. E., D. P. Schwartz, and D. H. Oppenheimer (1991), Slip rate, earthquake recurrence, and seismogenic potential of the Rodgers Creek fault zone, northern California: initial results, *J. Geophys. Res.*, *18*, 447–450.

Bürgmann, R., M. G. Kogan, G. M. Steblov, G. Hilley, V. E. Levin, and E. Apel (2005), Interseismic coupling and asperity distribution along the Kamchatka subduction zone, *J. Geophys. Res.*, *110*, B07405, doi:10.1029/2005JB003648.

Cakir, Z., A. M. Akoglu, S. Belabbes, S. Ergintav, and M. Meghraoui (2005), Creeping along the Ismetpasa section of the North Anatolian fault (western Turkey): Rate and extent from InSAR, *Earth Planet. Sci. Lett.*, *238*, 225–234, doi:10.1016/j.epsl.2005.06.044.

Cluff, L. S., and K. V. Steinbrugge (1966), Hayward fault slippage in the Irvington-Niles districts of Fremont, California, *Bull. Seismol. Soc. Am.*, *56*, 257–279.

d'Alessio, M. A., I. A. Johanson, R. Bürgmann, D. A. Schmidt, and M. H. Murray (2005), Slicing up the San Francisco Bay Area: Block kinematics and fault slip rates from GPS-derived surface velocities, *J. Geophys. Res.*, *110*, B06403, doi:doi:10.102/2004JB003496.

Dieterich, J. H. (1978), Time-dependent friction and the mechanics of stick-slip, *Pure. Appl. Geophys.*, *116*, 790–806.

Farr, T., and M. Kobrick (2000), Shuttle Radar Topography Mission produces a wealth of data, *Eos Trans. AGU*, *81*, 583–585.

Fattahi, H., and F. Amelung (2016), InSAR observations of strain accumulation and fault creep along the Chaman fault system, Pakistan and Afghanistan, *Geophys. Res. Lett.*, *43*, 8399–8406, doi:10.1002/2016GL070121.

Ferretti, A. (2014), *Satellite InSAR data: reservoir modeling from space*, 160 pp., European Assoc. Geosci. Eng., Houten, The Netherlands.

Ferretti, A., C. Prati, and F. Rocca (2001), Permanent scatterers in SAR interferometry, *IEEE Trans. Geosci. Remote Sensing*, *39*, 8–20.

Ferretti, A., F. Novali, R. Bürgmann, G. Hilley, and C. Prati (2004), InSAR permanent scatterer analysis reveals ups and downs in the San Francisco Bay Area, *Eos Trans. AGU*, *85*(34), 317.

Field, E. H., R. J. Arrowsmith, G. P. Biasi, P. Bird, T. E. Dawson, K. R. Felzer, D. D. Jackson, K. M. Johnson, T. H. Jordan, C. Madden, A. J. Michael, K. R. Milner, M. T. Page, T. Parsons, P. M. Powers, B. E. Shaw, W. R. Thatcher, R. J. Weldon, and Y. Zeng

(2014), Uniform California Earthquake Rupture Forecast, version 3 (UCERF3) – the time-independent model, *Bull. Seismol. Soc. Am.*, *104*, 1122–1180.

Floyd, M. A., G. J. Funning, J. R. Murray, J. L. Svarc, T. Herring, I. A. Johnason, J. Swiatlowski, K. Materna, C. W. Johnson, O. S. Boyd, J. M. Sutton, and E. Phillips (2014), Surface deformation before, during and after the 2014 south napa, california, earthquake from a spatially dense network of survey and continuous gps sites, abstract S33F-4904 presented at 2014 Fall Meeting, AGU, San Francisco, Calif., 15-19 Dec.

Floyd, M. A., R. J. Walters, J. R. Elliott, G. J. Funning, J. L. Svarc, J. R. Murray, A. J. Hooper, Y. Larsen, P. Marinkovich, R. Bürgmann, I. A. Johnason, and T. J. Wright (2016), Spatial variations in fault friction related to lithology from rupture and afterslip of the 2014 South Napa, California, earthquake, *Geophys. Res. Lett.*, *43*, 6808–6816, doi:10.1002/2016GL069428.

Funning, G. J., B. Parsons, T. J. Wright, J. A. Jackson, and E. J. Fielding (2005), Surface displacements and source parameters of the 2003 Bam (Iran) earthquake from Envisat advanced synthetic aperture radar imagery, *J. Geophys. Res.*, *110*(B09406), doi:10.1029/2004JB003,338.

Funning, G. J., R. Bürgmann, A. Ferretti, F. Novali, and A. Fumagalli (2007), Creep on the Rodgers Creek fault, northern San Francisco Bay area, from a 10-year PS-InSAR dataset, *Geophys. Res. Lett.*, *34*, L19306, doi:10.1029/2007GL030836.

Galehouse, J. S., and J. J. Lienkaemper (2003), Inferences drawn from two decades of alinement array measurements of creep on faults in the San Francisco Bay region, *Bull. Seismol. Soc. Am.*, *93*(6), 2415–2433.

Graymer, R. W., B. C. Moring, G. J. Saucedo, C. M. Wentworth, E. E. Brabb, and K. L. Knudsen (2006), Geologic map of the San Francisco Bay Region, *Sci. Invest. Map 2918*, U.S. Geol. Surv., Menlo Park, Calif.

Harsh, P. W., E. H. Pampeyan, and J. M. Coakley (1978), Slip on the Willits fault, California, *Earthquake Notes*, *49*, 22.

Hecker, S., D. Pantosti, D. P. Schwartz, J. C. Hamilton, L. M. Reidy, and T. J. Powers (2005), The most recent large earthquake on the Rodgers Creek fault, San Francisco Bay Area, *Bull. Seismol. Soc. Am.*, *95*, 844–860.

Hecker, S., V. E. Langenheim, R. A. Williams, C. S. Hitchcock, and S. B. DeLong (2016), Detailed mapping and rupture implications of the 1 km releasing bend in the Rodgers Creek fault at Santa Rosa, northern California, *Bull. Seismol. Soc. Am.*, *106*, 20 pp., doi:10.1785/0120150152.

Hooper, A. (2010), StaMPS/MTI 3.2 manual, accessed August 18, 2016 from http://homepages.see.leeds.ac.uk/ earahoo/stamps/.

Hooper, A., H. Zebker, P. Segall, and B. Kampes (2004), A new method for measuring deformation on volcanoes and other natural terrains using InSAR persistent scatterers, *Geophys. Res. Lett.*, *31*(L23611), doi:10.1029/2004GL021,737.

Hooper, A., P. Segall, and H. Zebker (2007), Persistent scatterer InSAR for crustal deformation analysis with application to Volcán Alcedo, Galápagos, *J. Geophys. Res.*, *112*(B07407), doi:10.1029/2006JB004,763.

Hooper, A., D. Bekaert, K. Spaans, and M. Arikan (2012), Recent advances in SAR interferometry time series analysis for measuring crustal deformation, *Tectonophys.*, *514–517*, 1–13.

Hsu, L., , and R. Bürgmann (2006), Surface creep along the Longitudinal Valley fault, Taiwan from InSAR measurements, *Geophys. Res. Lett.*, *33*, L06312, doi: 10.1029/2005GL024624.

Johanson, I. A., E. J. Fielding, F. Rolandone, and R. Bürgmann (2006), Coseismic and postseismic slip of the 2004 Parkfield earthquake from space-geodetic data, *Bull. Seismol. Soc. Am.*, *96*, S269–S282.

Jolivet, R., C. Lasserre, M.-P. Doin, S. Guillaso, G. Peltzer, R. Dailu, and J. Sun (2012), Shallow creep on the Haiyuan fault (Gansu, China), revealed by SAR interferometry, *J. Geophys. Res.*, *117*, B06401, doi:10.1029/2011JB008732.

Jolivet, R., C. Lasserre, M.-P. Doin, G. Peltzer, J.-P. A. J. Sun, and R. Dailu (2013), Spatio-temporal evolution of aseismic slip along the Haiyuan fault, China: Implications for fault frictional properties, *Earth Planet. Sci. Lett.*, *377–378*, 23–33, doi: 10.1016/j.epsl.2013.07.020.

Jónsson, S., H. Zebker, P. Segall, and F. Amelung (2002), Fault slip distribution of the 1999 Mw 7.1 Hector Mine earthquake, California, estimated from satellite radar and GPS measurements, *Bull. Seismol. Soc. Am.*, *92*(4), 1,377–1,389.

Kampes, B. M. (2006), *Radar interferometry: Persistent Scatterer technique*, Springer, Netherlands.

Kyriakopoulos, C., and A. V. Newman (2016), Structural asperity focusing locking and earthquake slip along the Nicoya megathrust, Costa Rica, *J. Geophys. Res.*, *121*, 5461–5476, doi:10.1002/2016JB012886.

Langenheim, V. E., C. W. Roberts, C. A. McCabe, D. K. McPhee, J. E. Tilden, and R. C. Jachens (2006), Preliminary isostatic gravity map of the Sonoma Volcanic Field and vicinity, Sonoma and Napa Counties, California, *U. S. Geological Survey Open File Report*, *06-1056*.

Lienkaemper, J. J. (2006), Digital database of recently active traces of the Hayward fault, California, *Open File Rep. 2006-177*, U.S. Geol. Surv., Menlo Park, Calif.

Lienkaemper, J. J., G. Borchardt, and M. Lisowski (1991), Historic creep rate and potential for seismic slip along the Hayward fault, California, *J. Geophys. Res.*, *96*, 18,261–18,283.

Lienkaemper, J. J., J. S. Galehouse, and R. W. Simpson (1997), Creep response of the Hayward fault to stress changes caused by the Loma Prieta earthquake, *Science*, *276*, 2014–2016.

Lienkaemper, J. J., S. B. DeLong, C. J. Domrose, and C. M. Rosa (2016), Afterslip behavior following the 2014 m 6.0 South Napa earthquake with implications for afterslip forecasting on other seismogenic faults, *Seismol. Res. Lett.*, *87*, 11 pp, doi: 10.1785/0220150262.

Lockner, D. A., C. Morrow, D. Moore, and S. Hickman (2011), Low strength of deep San Andreas fault gouge from SAFOD core, *Nature*, *472*, 82–85, doi:10.1038/nature09927.

Louie, J. N., C. R. Allen, D. C. Johnson, P. C. Haase, and S. N. Cohn (1985), Fault slip in southern California, *Bull. Seismol. Soc. Am.*, *75*, 811–833.

Lozos, J. C., R. A. Harris, J. R. Murray, and J. J. Lienkaemper (2015), Dynamic rupture models of earthquakes on the Bartlett Springs Fault, Northern California, *Geophys. Res. Lett.*, *42*, 4343–4349, doi:doi:10.1002/2015GL063802.

McFarland, F. S., J. J. Lienkaemper, and S. J. Caskey (2016), Data from theodolite measurements of creep rates on San Francisco Bay region faults, California, *Open File*

Rep. 2009-1119 v1.8, U.S. Geol. Surv., Menlo Park, Calif.

McLaughlin, R. J., V. E. Langenheim, A. M. Sarna-Wojcicki, R. J. Fleck, D. K. McPhee, C. W. Roberts, C. A. McCabe, and E. Wan (2008), Geologic map of the San Francisco Bay Region, *Open File Rep. 2008–1009*, U.S. Geol. Surv., Menlo Park, Calif.

McPhee, D. K., V. E. Langenheim, and R. C. Jachens (2007), Basin structure beneath the Santa Rosa Plain, northern California: implications for damage caused by the 1969 Santa Rosa and 1906 San Francisco earthquakes, *Bull. Seismol. Soc. Am.*, *97*, 1449–1457.

Michel, R., J.-P. Avouac, and J. Taboury (1999), Measuring ground displacements from SAR amplitude images: application to the Landers earthquake, *Geophys. Res. Lett.*, *26*, 875–878.

Moore, D. E., and D. A. Lockner (2013), Chemical controls on fault behavior: Weakening of serpentinite sheared against quartz-bearing rocks and its significance for fault creep in the san andreas system, *J. Geophys. Res.*, *118*, 1–13, doi:10.1002/jgrb.50140.

Moore, D. E., and M. J. Rymer (2007), Talc-bearing serpentinite and the creeping section of the San Andreas fault, *Nature*, *448*, 795–797.

Murray, J. R., and J. Langbein (2006), Slip on the San Andreas fault at Parkfield, California over two earthquake cycles and the implications for seismic hazard, *Bull. Seismol. Soc. Am.*, *96*, S283–S303.

Nason, R. D. (1971), Investigation of fault creep slippage in northern and central california, Ph.D. thesis, Univ. of Calif., San Diego, USA.

Peltzer, G., F. Crampé, and G. King (1999), Evidence of nonlinear elasticity of the crust from the Mw 7.6 Manyi (Tibet) earthquake, *Science*, *286*, 272–276.

Prescott, W. H., J. C. Savage, J. L. Svarc, and D. Manaker (2001), Deformation across the Pacific-North America boundary near San Francisco, California, *J. Geophys. Res.*, *106*(B4), 6,673–6,682.

Reid, H. (1910), The mechanics of the earthquake, in *The California Earthquake of 18 April, 1906: Report of the State Earthquake Investigation Commission, 2*, Carnegie Institution, Washington.

Rousset, B., R. Jolivet, M. Simons, C. Lasserre, B. Riel, P. Milillo, Z. Cakir, and F. Renard (2016), An aseismic slip transient on the North Anatolian fault, *Geophys. Res. Lett.*, *43*, 3254–3262, doi:10.1002/2016GL068250.

Ruina, A. (1983), Slip instability and state variable friction laws, *J. Geophys. Res.*, *88*, 10,359–10,370.

Schwartz, D. P., D. Pantosti, S. Hecker, K. Okumura, K. E. Budding, and T. Powers (1992), Late Holocene behavior and seismogenic potential of the Rodgers Creek fault zone, Sonoma County, California, in *Proceedings of the Second Conference on earthquake hazards in the eastern San Francisco Bay Area*, *California Department of Conservation, Division of Mines and Geology Special Publication*, vol. 113, edited by G. Borchardt, pp. 393–398.

Sleep, N. H., and M. L. Blanpied (1992), Creep, compaction and the weak rheology of major faults, *Nature*, *359*, 687–692.

Steinbrugge, K. V., E. G. Zacher, D. Tocher, C. A. Whitten, and C. N. Claire (1960), Creep on the San Andreas fault, *Bull. Seismol. Soc. Am.*, *50*, 389–415.

U.S. Geological Survey, and California Geological Survey (2006), Quaternary fault and fold database for the United States, accessed August 15, 2016 from http//earthquake.usgs.gov/regional/qfaults/.

Wallace, L. M., J. Beavan, R. McCaffrey, and D. Darby (2004), Subduction zone coupling and tectonic block rotations in the North Island, New Zealand, *J. Geophys. Res.*, *109*, B12406, doi:10.1029/2004JB003241.

Weldon, R. J., D. A. Schmidt, L. A. Austin, E. M. Weldon, and T. E. Dawson (2013), Appendix D: Compilation of creep rate data for california faults and calculation of moment reduction due to creep, in *The Uniform California Earthquake Rupture Forecast, version 3 (UCERF 3)*, p. 43 pp., U.S. Geol. Surv. Open-File Rept. 2013-1165-D, and California Geol. Surv. Special Rept. 228-D.

Wells, D., and K. Coppersmith (1994), New empirical relationships among magnitude, rupture length, rupture width, rupture area, and surface displacement, *Bull. Seismol. Soc. Am.*, *84*(4), 974–1002.

Wessel, P., and W. H. F. Smith (1998), New, improved version of generic mapping tools released, *Eos Trans. AGU*, *79*, 579.

Wisely, B. A., D. A. Schmidt, and R. J. Weldon (2008), Appendix P: Compilation of surface creep on California faults and comparison of WGCEP 2007 deformation model to Pacific-North American Plate motion, in *The Uniform California Earthquake Rupture Forecast, version 2 (UCERF 2)*, p. 43 pp., U.S. Geological Survey OpenFile Report 2007-1437P and California Geological Survey Special Report 203P.

Wong, I. G., and J. D. J. Bott (1995), A new look back at the 1969 Santa Rosa, California, earthquakes, *Bull. Seismol. Soc. Am.*, *85*(1), 334–341.

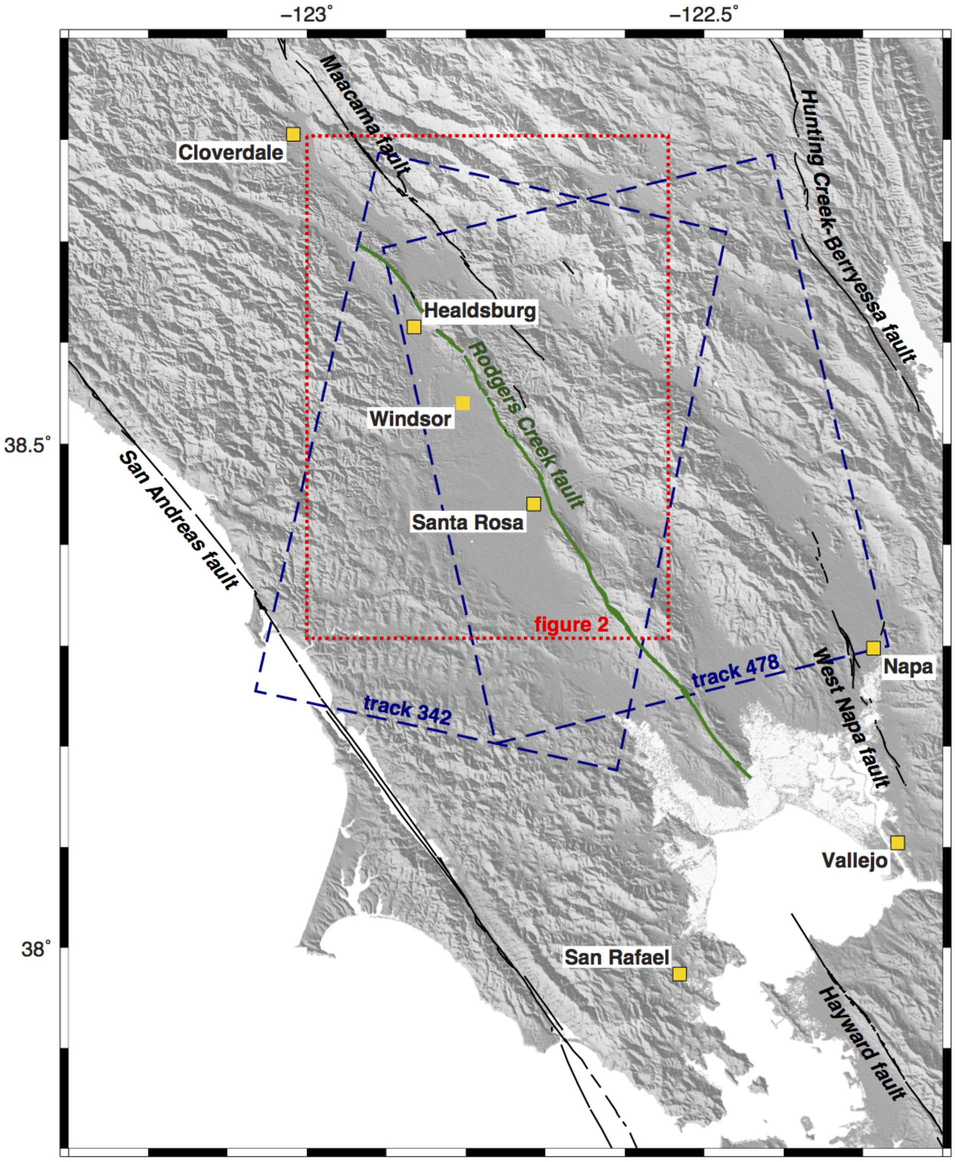

Figure 1. Location map of study area in northern California. The Rodgers Creek fault trace is marked in green, other major faults in black [*U.S. Geological Survey and California Geological Survey*, 2006]. Locations of significant cities are marked with yellow squares; previous work suggests that creep may be present on the Rodgers Creek fault between Santa Rosa and Healdsburg [e.g. *Funning et al.*, 2007]. Blue dashed rectangles indicate the coverage of the two Envisat persistent scatterer InSAR data sets (track 342 descending, track 478 ascending). Red dotted rectangle delimits the area shown in Figure 2.

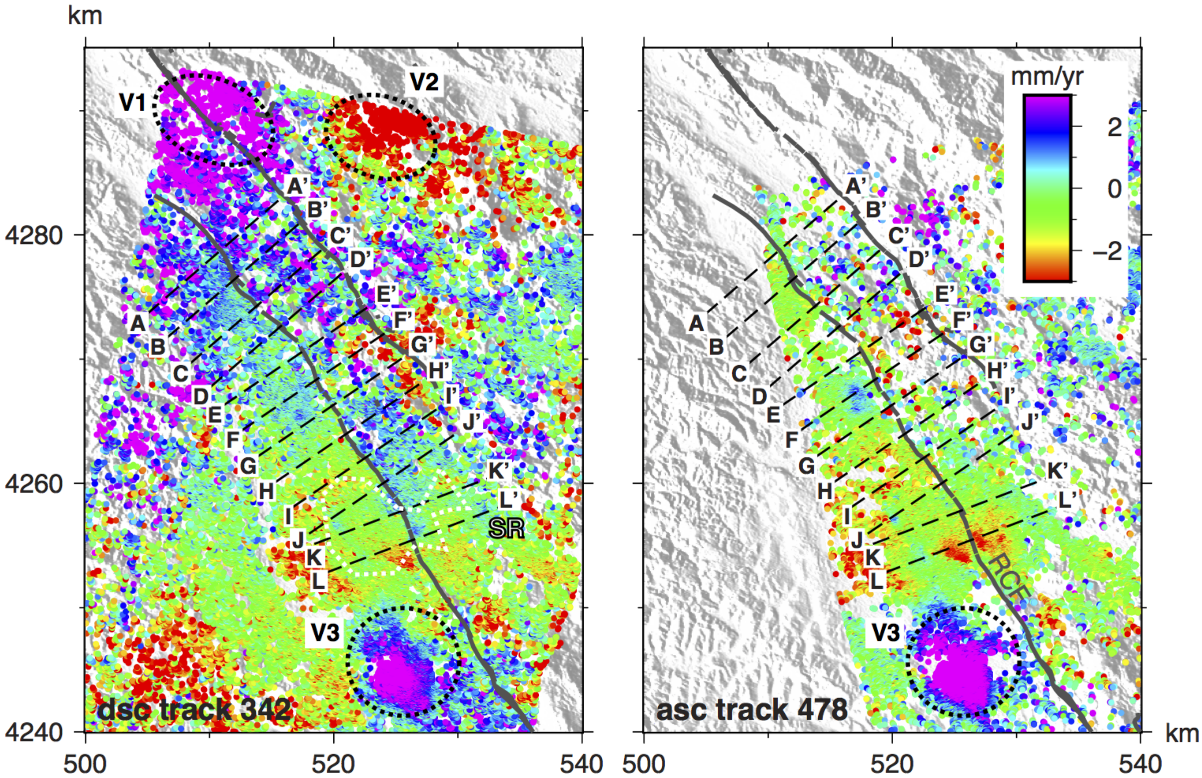

Figure 2. Persistent scatterer InSAR data covering the Rodgers Creek fault. Data shown are best-fitting linear velocities for Envisat data acquired in the period 2003–2010 from descending track 342 (dsc, left) and ascending track 478 (asc, right), processed using the StaMPS software [*Hooper et al.*, 2004, 2007]. Negative velocities (red) indicate movement of the ground away from the satellite, positive velocites (blue) represent movement towards the satellite. Gray solid lines indicate locations of major faults [RCF: Rodgers Creek fault], black dashed lines the locations of profiles shown in Figure 4. Dotted black lines indicate velocity features V1–V3 described in the main text. White dotted line indicates the outline of Santa Rosa [SR]. Coordinates shown here are in UTM km, zone 10; area covered by figure shown in Figure 1.

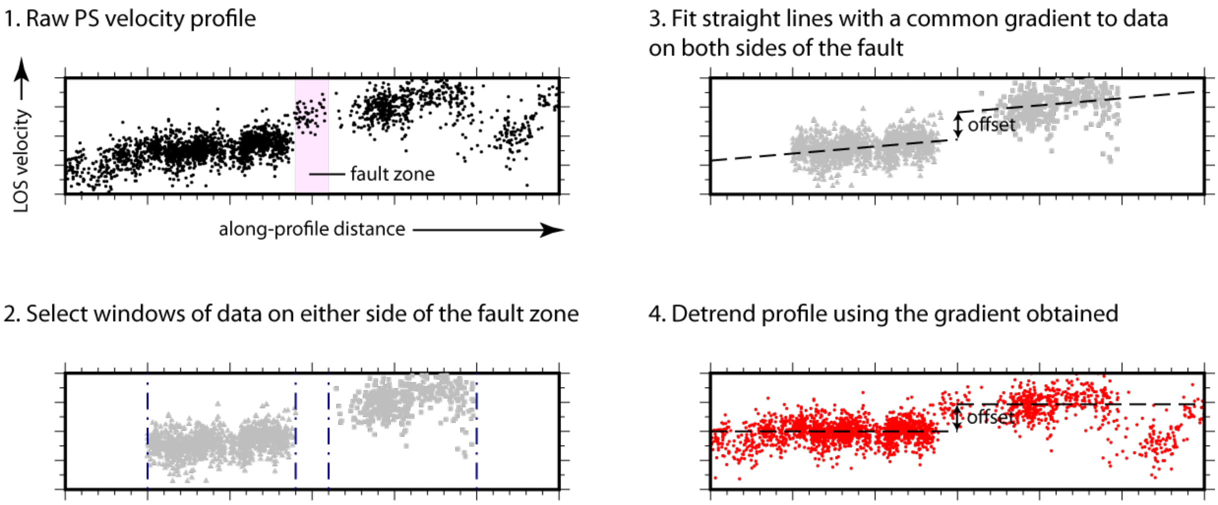

Figure 3. Schematic showing the process of estimating line-of-sight offset rates from persistent scatterer InSAR profiles. Straight lines with a common gradient are fitted to windows of data selected from either side of the approximate fault location. The offset rate is the vertical distance between the two lines on the profile.

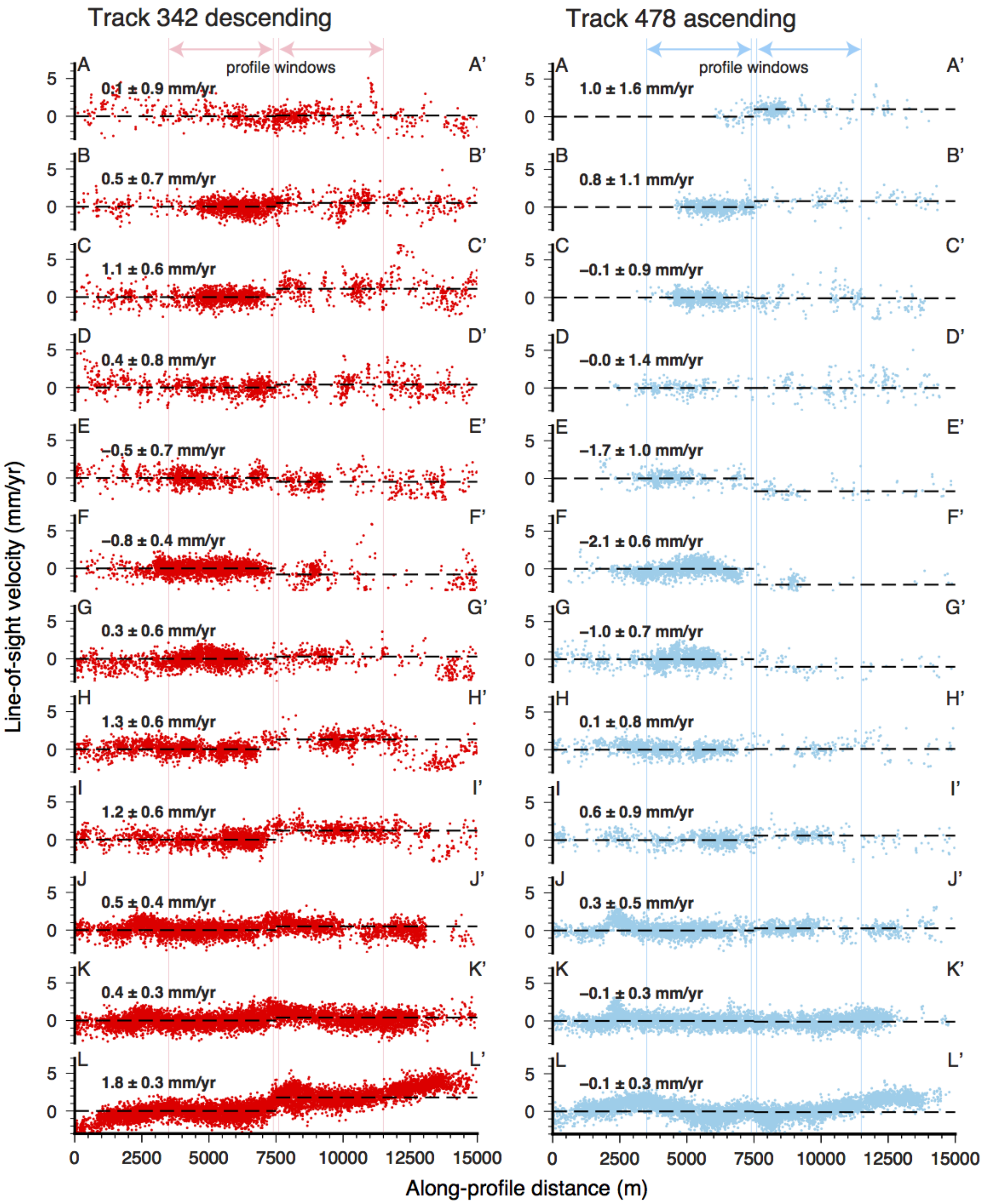

Figure 4. Detrended InSAR line-of-sight velocity profiles for the Envisat descending track 342 data (left) and ascending track 478 data (right). Offsets are estimated using the procedure shown in Figure 3 and are provided with their formal two-sigma uncertainties. A window of data extending 4 km from the fault in both directions is used, data within 100 m of the fault are excluded. Offsets are estimated using the procedure shown in Figure 3 and are provided with their formal two-sigma uncertainties. Profile locations are given in Figure 2.

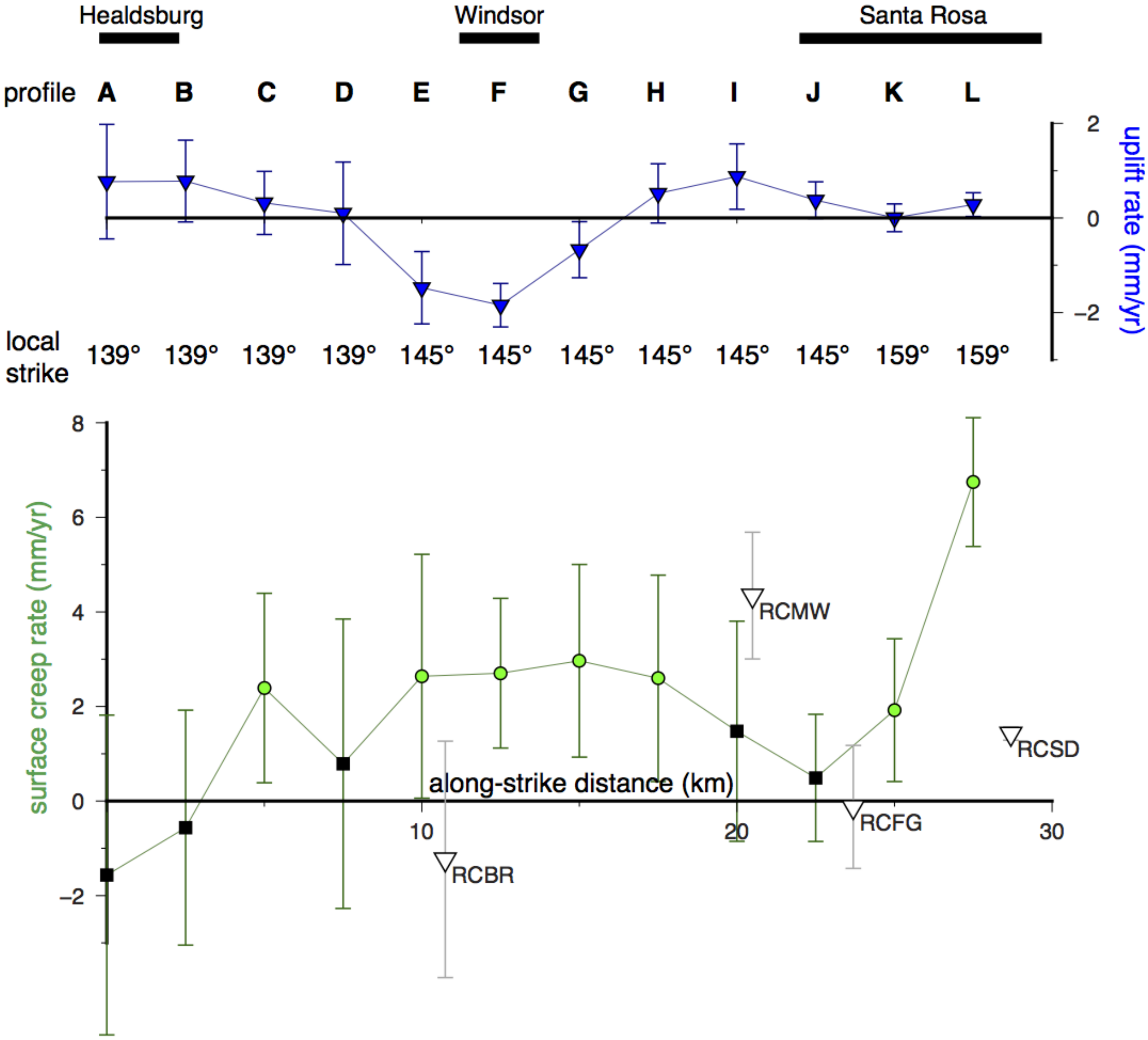

Figure 5. Creep and uplift rate distribution along the northern Rodgers Creek fault. Plotted are right-lateral fault offset rates ('surface creep rates', bottom) and vertical fault offset rates ('uplift rates', representing east side-up movement, top) estimated from decomposition of line-of-sight offset rates, with two-sigma uncertainties (95% confidence intervals) from propagating uncertainties through the calculations. Two portions of the fault – within the city of Santa Rosa, and a section starting ∼ 5 km to the northwest – have creep rates that are more than two sigmas above zero, indicating with high confidence that they are creeping (green circles). These estimates are compared with alinement array measurements [white triangles *McFarland et al.*, 2016]. In general, where InSAR and alinement array observations overlap in space, their uncertainties also overlap, indicating that the observations are compatible, although in the case of RCMW, that overlap is very small. [Temporal coverage of each observation set: Envisat InSAR data, 2003–2010; RCBR (Brooks Rd), 2010–2015; RCMW (Mark West Springs Rd), 2008–2015; RCFG (Fountaingrove Blvd), 2008–2011; RCSD (Solano Dr), 2002–2015]

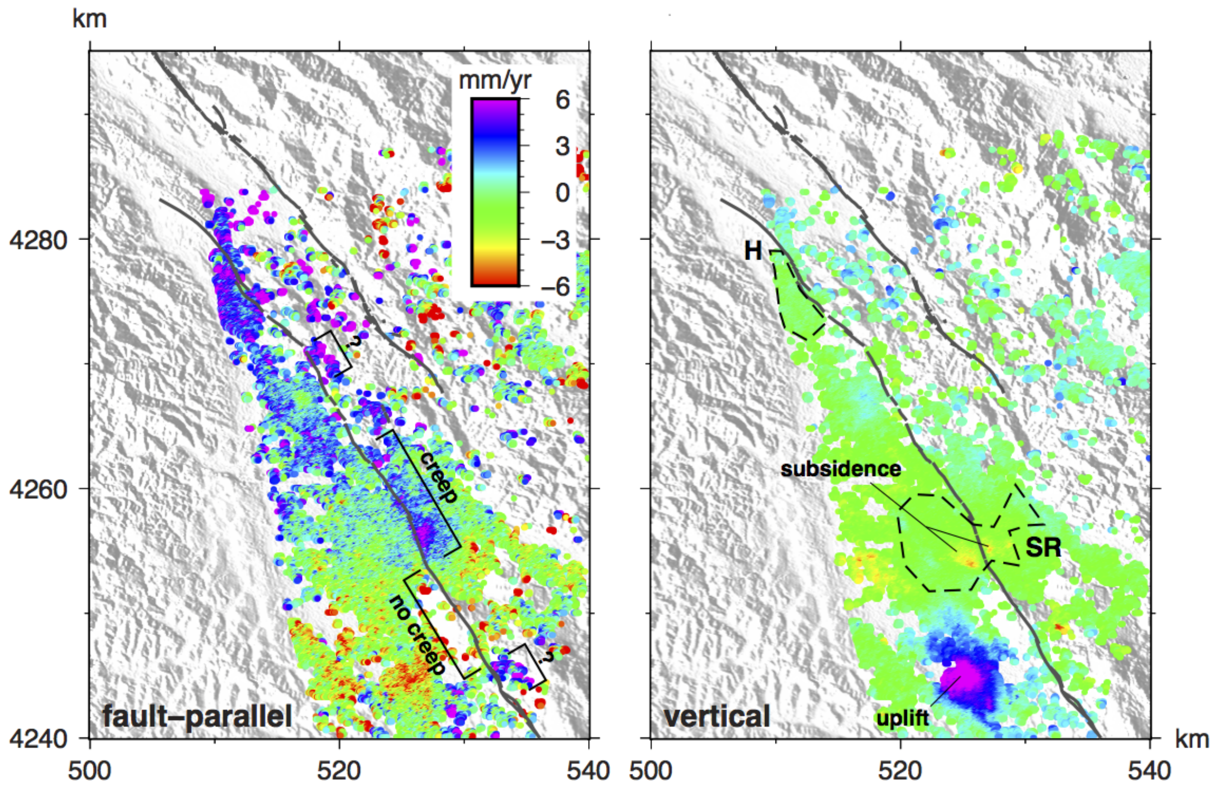

Figure 6. Map pattern of surface deformation velocities, decomposed into fault-parallel (left) and vertical (right) components. Fault-parallel velocities are horizontal velocities with an azimuth of 135°, i.e. positive fault-parallel velocities indicate movement to the southeast. An abrupt increase in velocity from west to east across the Rodgers Creek fault is consistent with right-lateral creep, such as a $\sim$ 10 km zone extending northwest along-strike from Santa Rosa, and also possibly in two other localized zones (indicated by question marks). In contrast, there is no evidence for creep immediately southeast of Santa Rosa. In the vertical deformation map, positive deformation rates indicate uplift; the most prominent feature is an uplift feature with an amplitude of 6 mm/yr in the southern part of the image, that we interpret as a recharging aquifer. We can also identify localized subsidence features across the area, such as a pair of subsiding areas either side of the Rodgers Creek fault in Santa Rosa. [Black dashed lines indicate locations of cities. SR: Santa Rosa, H: Healdsburg.]

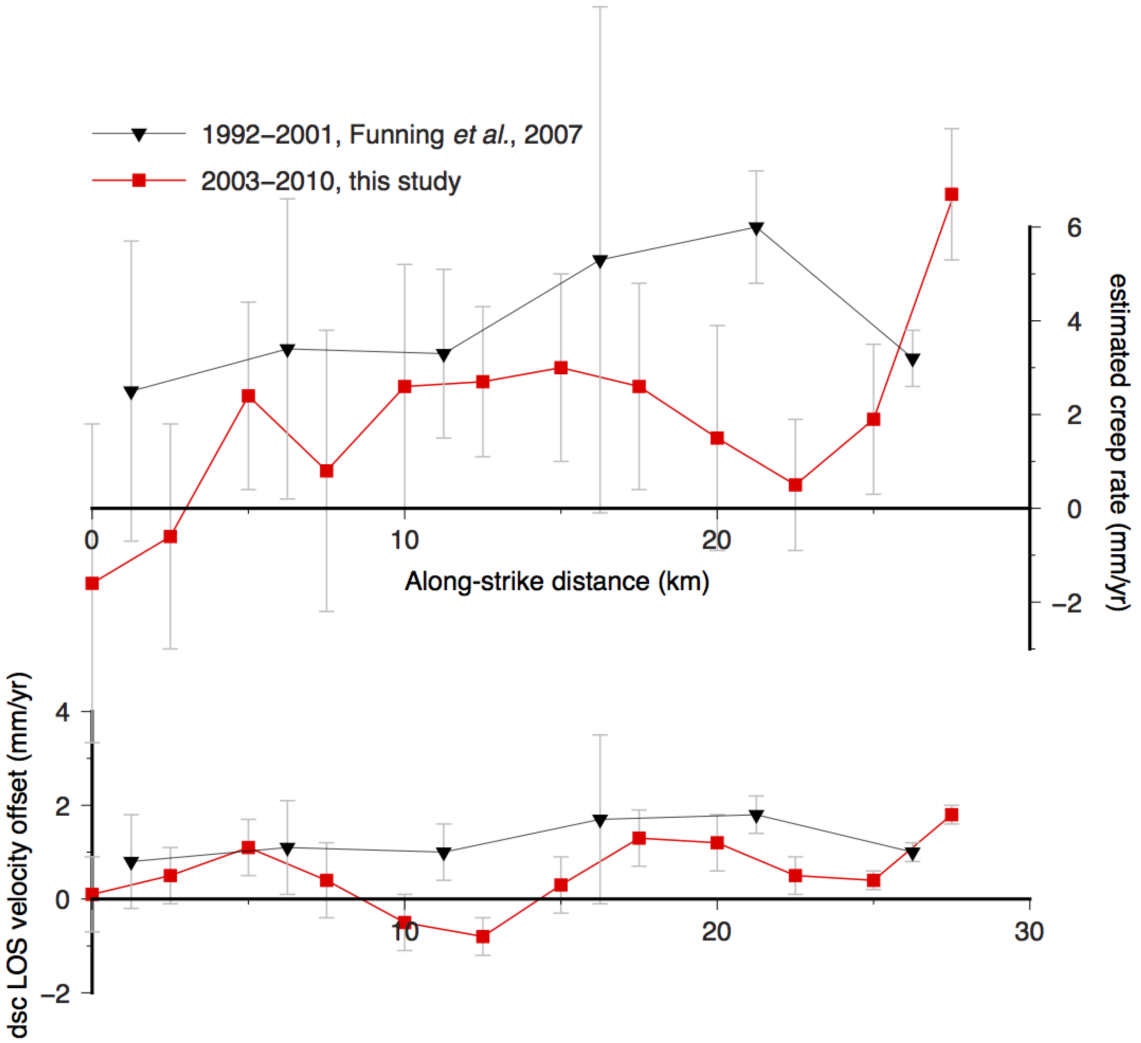

Figure 7. Comparison of estimated creep rates (top) and line-of-sight velocity offsets (bottom) with results from an earlier study. Black symbols/lines are the results of *Funning et al.* [2007], where data from the ERS satellites from 1992–2001 were used and only descending (dsc) track data were used to estimate creep rates. Red symbols/lines are the corresponding quantities from this study, spanning 2003–2010, where both descending and ascending track data are used in the creep rate estimation. Error bars represent two-sigma uncertainties. The estimated creep rates in the range 17–23 km along-strike differ by ~ 5 mm/yr, however the line-of-sight velocity offsets at the same locations are similar. This indicates that the creep rates from the earlier study may be erroneously high due to a lack of ascending data used in the analysis, and that the creep rates may in fact be similar between the decades.

Table 1. Creep rate estimates from profile offsets.

Profile	Distance[a] (km)	Descending rate[b c] (mm/yr)	Ascending rate[b c] (mm/yr)	Creep rate[c d] (mm/yr)	P^e (creep rate > 0)	Vertical rate[c f] (mm/yr)
A–A'	0	0.1 ± 0.9	1.0 ± 1.6	-1.6 ± 3.4	0.18	0.8 ± 1.2
B–B'	2.5	0.5 ± 0.7	0.8 ± 1.1	-0.6 ± 2.5	0.33	0.8 ± 0.9
C–C'	5.0	1.1 ± 0.6	-0.1 ± 0.9	2.4 ± 2.0	0.99	0.3 ± 0.7
D–D'	7.5	0.4 ± 0.8	0.0 ± 1.4	0.8 ± 3.1	0.70	0.1 ± 1.1
E–E'	10.0	-0.5 ± 0.7	-1.7 ± 1.0	2.6 ± 2.6	0.98	-1.5 ± 0.8
F–F'	12.5	-0.8 ± 0.4	-2.1 ± 0.6	2.7 ± 1.6	> 0.99	-1.8 ± 0.5
G–G'	15.0	0.3 ± 0.6	-1.0 ± 0.7	3.0 ± 2.0	0.99	-0.7 ± 0.6
H–H'	17.5	1.3 ± 0.6	0.1 ± 0.8	2.6 ± 2.2	0.99	0.5 ± 0.6
I–I'	20.0	1.2 ± 0.6	0.6 ± 0.9	1.5 ± 2.3	0.90	0.9 ± 0.7
J–J'	22.5	0.5 ± 0.4	0.3 ± 0.5	0.5 ± 1.3	0.77	0.4 ± 0.4
K–K'	25.0	0.4 ± 0.3	-0.1 ± 0.3	1.9 ± 1.5	0.99	0.0 ± 0.3
L–L'	27.5	1.8 ± 0.3	-0.1 ± 0.3	6.7 ± 1.4	> 0.99	0.3 ± 0.3

[a] Distance southeastwards along strike from profile A–A', near Healdsburg.

[b] Line-of-sight offset rates of the east side of the fault with respect to the west side.

[c] All quoted uncertainties are 2σ formal uncertainties from propagation of errors through the profile fitting and velocity decomposition calculations.

[d] Right-lateral horizontal offset rates, estimated in the local strike direction.

[e] One-tailed Gaussian probability that the creep rate is right-lateral and greater than zero. $P > 0.99$ indicates a preferred creep rate value that is more than three standard deviations above zero.

[f] Vertical offset rates, where positive values indicate uplift of the east side of the fault with respect to the west.